

Chemical Science

Accepted Manuscript

This article can be cited before page numbers have been issued, to do this please use: S. Yan, Z. Tang, Z. Yang, Y. Zhang, Y. Zhu, X. Qiu, X. Zhang, D. Wang, K. Hou, J. Zhang, C. Long, J. Han and Y. Yuan, *Chem. Sci.*, 2020, DOI: 10.1039/D0SC01202E.



This is an Accepted Manuscript, which has been through the Royal Society of Chemistry peer review process and has been accepted for publication.

Accepted Manuscripts are published online shortly after acceptance, before technical editing, formatting and proof reading. Using this free service, authors can make their results available to the community, in citable form, before we publish the edited article. We will replace this Accepted Manuscript with the edited and formatted Advance Article as soon as it is available.

You can find more information about Accepted Manuscripts in the [Information for Authors](#).

Please note that technical editing may introduce minor changes to the text and/or graphics, which may alter content. The journal's standard [Terms & Conditions](#) and the [Ethical guidelines](#) still apply. In no event shall the Royal Society of Chemistry be held responsible for any errors or omissions in this Accepted Manuscript or any consequences arising from the use of any information it contains.

ARTICLE

Reconstructed porous copper surface promotes selectivity and efficiency toward C₂ products by electrocatalytic CO₂ reductionJianyu Han^a, Chang Long^{a,b}, Jing Zhang^c, Ke Hou^a, Yi Yuan^{a,d}, Dawei Wang^a, Xiaofei Zhang^{a,b}, Xueying Qiu^{a,b}, Yanfei Zhu^{a,e}, Yin Zhang^a, Zhongjie Yang^{a,e}, Shuhao Yan^{a,e}, Zhiyong Tang^{a,e*}Received 00th January 20xx,
Accepted 00th January 20xx

DOI: 10.1039/x0xx00000x

Electrocatalytic synthesis of multicarbon (C₂₊) products from CO₂ reduction suffers from poor selectivity and low energy efficiency. Herein, a facile oxidation-reduction cycling method is adopted to reconstruct the Cu electrode surface with the help of halide anions. The surface composed of entangled Cu nanowires with hierarchical pores is synthesized in presence of I⁻, exhibiting a C₂ Faradaic efficiency (FE) of 80% at -1.09 V vs. RHE. A partial current density of 21 mA/cm² is achieved with a C₂ half-cell power conversion efficiency (PCE) of 39% on this electrode. Such high selective C₂ production is explored to mainly originate from CO intermediate enrichment inside hierarchical pores rather than the surface lattice effect of Cu electrode.

Introduction

The electrochemical synthesis of value-added feedstocks by carbon dioxide (CO₂) reduction is an appealing approach for permanent storage of renewable electricity and closing carbon neutral cycle^{1, 2}. Multicarbon (C₂₊) products including ethylene, alcohol and propanol are highly desirable owing to their diverse applications in industry³⁻⁵. However, the multistep nature and the competing pathways make it a challenge to drive the reactions to the demanded C₂₊ products.

Copper (Cu) is so far known to be the most promising electrocatalyst that may improve the formation of C₂₊ products via CO₂ reduction^{6, 7}. One major approach attempting to endow Cu with the preference for C₂₊ products is to fabricate the oxide-derived Cu (OD-Cu) surfaces. The thermal oxidation^{8, 9}, anodic treatment^{10, 11}, electrodeposition^{12, 13} and hydrothermal¹⁴ synthesis have been reported to create surface oxide layers. Nevertheless, regardless of the methods employed, the enhanced C₂ selectivity is typically attributed to two mechanisms. One is that the residual subsurface Cu⁺ under the reduction conditions stabilizes the CO intermediates, thus lowering overpotential and boosting C₂ selectivity^{9, 15}; and the other is that the oxide-derived facets or undercoordinated surface Cu sites favor C₂ formation^{5, 16}.

We note that the reconstructed surface morphology of OD-Cu is seldom considered, which is essential in catalysis^{17, 18}. The

porous and inhomogeneous surfaces, which are generally generated upon rapid removal of lattice oxygen under a very negative reduction potential¹², would possess large surface roughness and hence benefit C₂₊ formation¹⁹. Previous studies have revealed that porous structures boost C₂₊ production from either CO or CO₂ electroreduction through a confinement effect²⁰⁻²².

In this work, the halide anions are utilized to reconstruct the Cu surface via electrochemical redox treatment. A Cu film consisting of entangled Cu nanowires (Re-Cu-I) is formed when I⁻ is involved, which morphology is rarely reported by the previous works adopting the similar method^{10, 11, 23-25}. It exhibits better selectivity toward C₂ generation compared with Cu nanoparticles obtained with Br⁻ and Cl⁻. It is found that the hierarchical pores rather than the reconstruction-derived property are responsible for this enhancement, which is distinct from the mechanism proposed in the literatures^{11, 23, 24}. The porous structure from the disordered accretion of Re-Cu-I is capable of enriching CO to enhance local *CO coverage at the surface, consequently boosting C₂ species generation. A C₂ Faradaic efficiency (FE) of 80% is achieved with a partial current density of 21 mA/cm² at -1.09 V vs. reversible hydrogen electrode (RHE), corresponding to a C₂ half-cell PCE of 39% on this electrode.

Results and discussion

Catalysts preparation and characterization

The surface of the polycrystalline electropolished Cu (EP-Cu) electrode is reconstructed by electrochemical oxidative-reductive cycling in 0.1 M KHCO₃ aqueous solution with help of halide anions (Fig. 1a). Without addition of potassium halides, a small redox wave with the current density in microampere per square centimeter is discerned, suggesting that electrode

^a CAS Key Laboratory of Nanosystem and Hierarchical Fabrication, CAS Center for Excellence in Nanoscience, National Center for Nanoscience and Technology, Beijing 100190, P. R. China.

^b School of Materials Science and Engineering, Harbin Institute of Technology, Harbin 150080, P. R. China.

^c Institute of Applied Chemistry, Shanxi University, Taiyuan 030006, P. R. China

^d School of Chemistry, Beihang University, Beijing 100083, P. R. China.

^e University of Chinese Academy of Sciences, Beijing 100049, P. R. China.

Electronic Supplementary Information (ESI) available: [details of any supplementary information available should be included here]. See DOI: 10.1039/x0xx00000x



surface reaction is mild (black curve in Fig. S1). Upon addition of KI, two orders of magnitude higher current density is observed at the oxidative potential (0.5 V to 0.8 V vs. RHE), which is ascribed to formation of CuI (purple curve in Fig. S1). The insoluble CuI emerged passivates the Cu electrode surface and consequently prevents further dissolution of Cu surface²³, causing a dramatically decreased current density at 0.9 V vs. RHE. As-generated Cu is then reduced at the potential ranging from 0.3 V to -0.3 V vs. RHE to form metallic Cu. As comparison, in the presence of KCl or KBr, the linearly increased current density is distinguished at the oxidative potential from 0.5 V to 0.9 V vs. RHE, indicating the continuous dissolution of Cu (green and orange curves in Fig. S1). Subsequently, as-dissolved Cu is transformed to Cu₂O and redeposited onto the electrode surface under reductive scan¹⁰, finally reducing to metallic Cu at more negative potential from -0.3 V to -0.6 V vs. RHE compared with the case in the presence of KI.

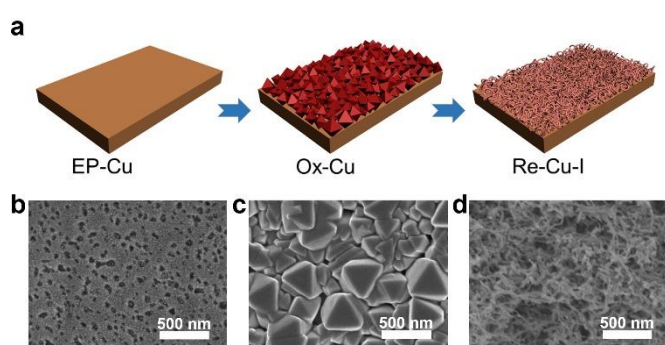


Fig. 1 Schematic illustration and morphology characterization of the surface reconstruction process. (a) Scheme of the electrochemical redox reconstruction process. SEM images of EP-Cu (b), Ox-Cu (c) and Re-Cu-I (d).

The grazing incident X-ray diffraction (GIXRD), scanning electron microscopy (SEM) and corresponding energy-dispersive X-ray spectroscopy (EDS) are conducted to monitor the phase transformation during the surface reconstruction process of Cu electrode in the presence of KI. Initially, a rather flat surface is observed for Cu electrode after being electropolished (EP) in phosphoric acid (Fig. 1b and Fig. S2). And the in-plane surface of EP-Cu is dominated by the Cu (200) facets (yellow curve in Fig. 2a). Under the oxidative condition, polyhedra are evidenced to fully cover the electrode surface (Fig. 1c). The SEM images and corresponding EDS elemental mapping indicate that these polyhedra are characteristic of Cu and I with a molar ratio of 2.7 to 1 (Fig. S3 and Table S1). The XRD pattern of the oxidized Cu (Ox-Cu) suggests that the in-plane surface consists of CuI and metallic Cu (pink curve in Fig. 2a). After the reductive potential is applied, Cu nanowires of diameters in 23.4 ± 5.9 nm (Re-Cu-I) are produced and entangled all around the surface, giving rise to a hierarchical porous structure (Fig. 1d and Fig. S4-S5). Only Cu and O are detected by EDS elemental mapping with a molar percentage of 88.2% and 10.8% (Fig. S6 and Table S1). After reduction, two phases are observed. The major Cu phase is dominated by Cu (220) along with Cu (200) facets, while the Cu₂O with (111) and (200) facets is the minor phase (purple curve in Fig. 2a).

Obviously different from the case with KI as electrolyte, rather dense structure consisted of quasi-cubic nanoparticles²⁵ obtained after electrochemical surface reconstruction of Cu electrode in the presence of KBr or KCl (Fig. S7-S10). And the molar percentage of O slightly increases with respect to that in the Re-Cu-I (Table S1). As displayed in Fig. S11, the XRD patterns show that the major phase in the Re-Cu-Br and Re-Cu-Cl is also metallic Cu accompanied with Cu₂O as the minor phase. The difference is that the Cu (200) is the dominated facet instead of Cu (220) in Re-Cu-I.

It has been known that the Cl⁻ promotes the Cu dissolution by chelating with Cu⁺ to form [CuCl₂]⁻ complexes whereas the I⁻ inhibits the Cu dissolution by generation of highly insoluble polyhedral CuI²⁶. Therefore, it can be concluded that the inhibitor nature of I⁻ and the promoter role of Br⁻ and Cl⁻ toward Cu dissolution cause the distinct oxidized intermediates and ultimately induce quite different structures on the Cu electrode surface.

The X-ray photoelectron spectroscopy (XPS) is performed to trace the oxidation state change of Cu during the reconstruction process. As shown in Fig. S12, a strong peak at 932.4 eV in the Cu 2p_{3/2} region is found for EP-Cu, Ox-Cu and Re-Cu-I, which is ascribed to Cu⁰ or Cu⁺²⁷. The absence of satellite peaks excludes the existence of Cu²⁺ species, in agreement with XRD results²⁴. The strong I 2p peak at 619 eV is discerned in Ox-Cu, further confirming formation of CuI in the oxidized state (Fig. S13). The reduced (but not eliminated) signal of I 2p peak in Re-Cu-I should come from I⁻ adsorbed on the surface of Cu electrode. Cu Auger spectra are also conducted to distinguish Cu⁰ from Cu⁺ in Re-Cu-I, Re-Cu-Br and Re-Cu-Cl. One main Auger peak at 568.1 eV corresponding to Cu⁰ and another small peak ascribed to Cu⁺ are observed for all the three samples²⁸ (Fig. S14). It suggests that all the three samples are composed of metallic Cu and Cu₂O, which is in good agreement with the Cu 2p XPS analysis.

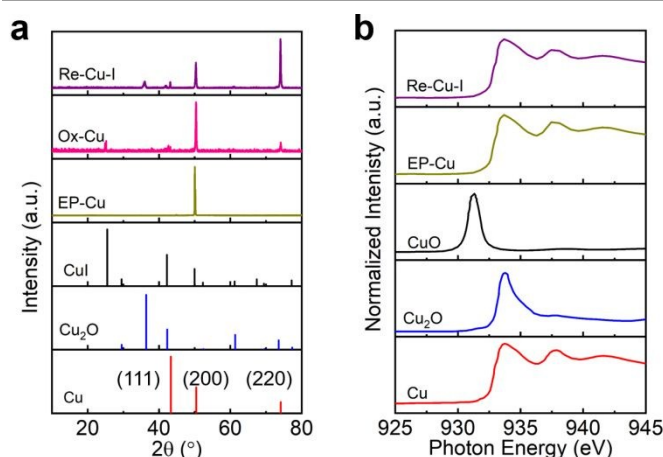


Fig. 2 Structural characterization of EP-Cu, Ox-Cu and Re-Cu-I. (a) GIXRD patterns of Re-Cu-I (purple), Ox-Cu (pink), EP-Cu (yellow) and reference samples CuI (black PDF#06-0246), Cu₂O (blue, PDF#05-0667), Cu (red, PDF#04-0836). (b) Cu L-edge XAS spectra of Re-Cu-I (purple), EP-Cu (yellow) and reference samples CuO (black), Cu₂O (blue) and Cu (red).



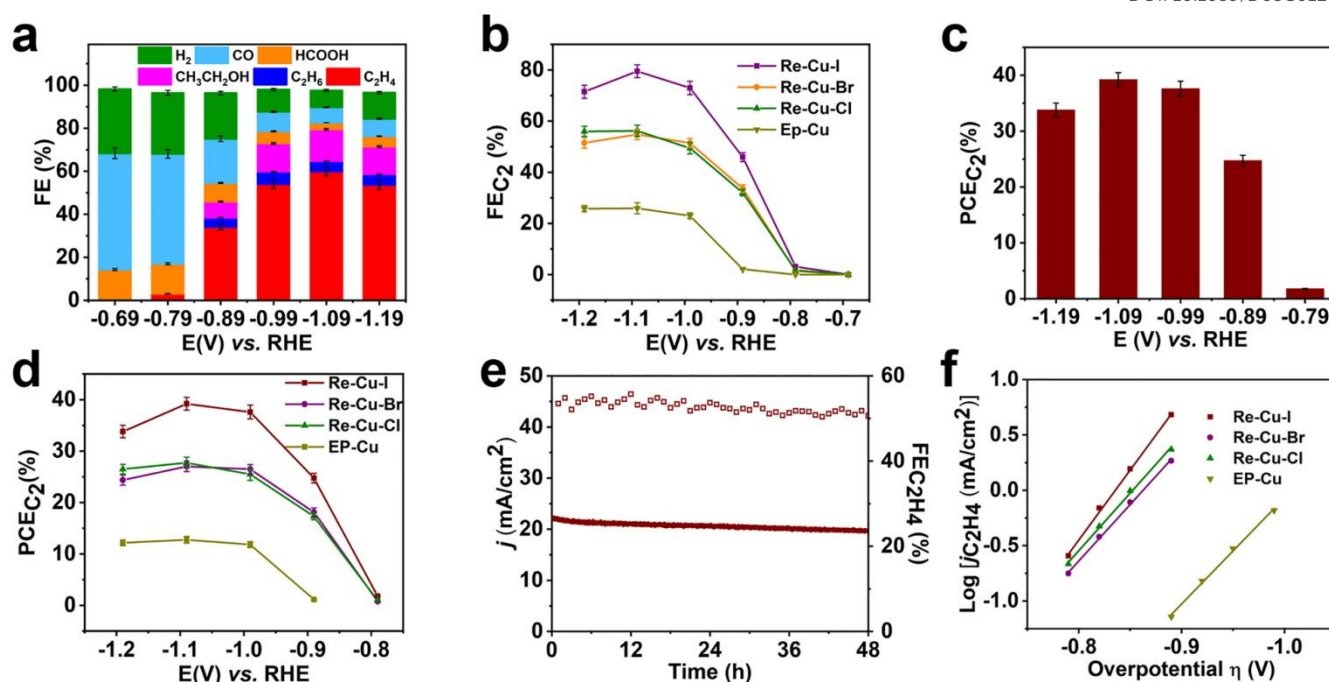


Fig. 3 Electrochemical CO_2 reduction performance of Re-Cu-I, Re-Cu-Br and Re-Cu-Cl. (a) FE of carbon products on Re-Cu-I at potential ranging from -0.69 V to -1.19 V vs. RHE. (b) FE of C_2 products on Re-Cu-I, Re-Cu-Br, Re-Cu-Cl and EP-Cu at potential ranging from -0.69 V to -1.19 V vs. RHE. (c) PCE of C_2 products on Re-Cu-I at potential ranging from -0.79 V to -1.19 V vs. RHE. (d) PCE of C_2 products on Re-Cu-I, Re-Cu-Br, Re-Cu-Cl and EP-Cu at potential ranging from -0.79 V to -1.19 V vs. RHE. (e) Long term measurement of Re-Cu-I for electrocatalytic CO_2 reduction at the potential of -0.99 V vs. RHE. (f) Tafel plot of C_2H_4 on Re-Cu-I, Re-Cu-Br, Re-Cu-Cl and EP-Cu for electrocatalytic CO_2 reduction.

The Cu L-edge X-ray absorption spectroscopy (XAS) that is more sensitive to the structural change is employed to estimate the Cu oxidation state in the Cu electrode²⁹. References samples including Cu, Cu_2O and CuO are also provided to quasi-quantitative analysis of the composition of the catalyst by linear combination fitting of the XAS data (Fig. 2b). The results demonstrate that the EP-Cu is fully in Cu^0 state (Table S2), and the Re-Cu-I contains 75% Cu^0 and 25% Cu^+ . The concentration of Cu^0 determined in Re-Cu-Br and Re-Cu-Cl is 63% and 67% respectively, where the rest Cu species are also Cu^+ species (Fig. S15 and Table S2). It deserves to be noted that the measured ratio between Cu^0 and Cu^+ is in good agreement for XAS and EDS characterizations (Table S3).

In short, the varied property of I^- with respect to Cl^- and Br^- leads to different redox behavior of Cu electrode, thus giving rise to distinct surface structure. XAS analysis confirms that Re-Cu-I, Re-Cu-Br, Re-Cu-Cl all consist of Cu^0 and Cu^+ with similar composition. Thus, it is beneficial for correlating the electrocatalytic performance of these three catalysts to their surface structures.

Electrocatalytic CO_2 reduction

To investigate the electrochemical performance of surface reconstructed Cu electrode, CO_2 reduction is conducted in 0.1 M KHCO_3 aqueous solution utilizing an H-cell configuration. Prior to the electrochemical collection, all the Cu electrodes are firstly activated by electrolysis at -0.99 V vs. RHE for 15 min to reduce the Cu^+ . The three electrodes after the electrolysis are composed of metallic Cu as evidenced by the Cu LMM spectra,

which rules out possible influence of Cu oxidation state (Fig. S16). Cyclic voltammetry (CV) curves of Re-Cu-I are firstly recorded in the above solution saturated with N_2 or CO_2 . As shown in Fig. S17, the current density under CO_2 atmosphere is 2 magnitudes higher than that under N_2 atmosphere, implying that the Re-Cu-I is an excellent catalyst for CO_2 reduction.

Controlled potential electrolysis is then carried out at the potential ranging from -0.69 V to -1.19 V vs. RHE in CO_2 saturate 0.1 M KHCO_3 (pH 6.8). The evolved gaseous products are analyzed and quantified by an online gas chromatograph (GC) while the liquid products are determined by ^1H NMR after the electrolysis. At an initial potential of -0.69 V, CO with Faradaic efficiency (FE) of 54.1% is detected as the major gaseous product and HCOOH with FE of 14.3% is liquid product accompanied with H_2 as a byproduct (Fig. 3a). The C_2H_4 begins to evolve at the potential of -0.79 V vs. RHE but the C_1 species are still the main products from CO_2 reduction. When more negative potential is applied, the FE of C_2H_4 dramatically increases to 54.1% at -0.99 V vs. RHE and reaches the optimal value of 59.9% at the potential of -1.09 V vs. RHE. FE of C_2H_4 is observed to slightly decrease to 53.6% under further negative potential of -1.19 V due to the CO_2 transportation limitation, which is also revealed by the current output (Fig. 3b). Noteworthy, at the potential of -1.09 V vs. RHE, the whole FE for C_2 species (FE_{C_2}) reaches 80% with a partial current density of 21 mA/cm^2 (Fig. 3b). Furthermore, the half-cell power conversion efficiency (PCE) of the entire C_2 species is up to 39% (Fig. 3c), which is among the highest reported value under neutral condition³⁰⁻³⁴ (Table S4).



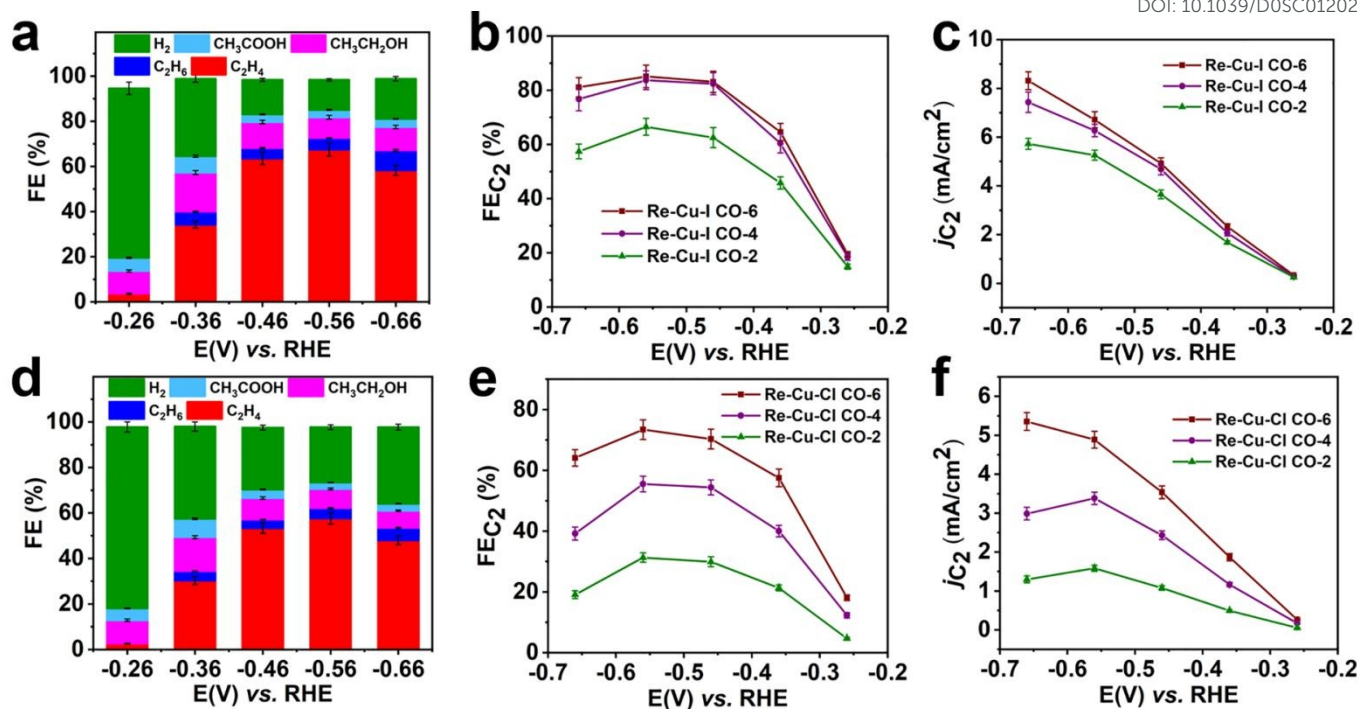


Fig. 4 Electrochemical CO reduction performance of Re-Cu-I, Re-Cu-Br and Re-Cu-Cl. FE of carbon products from CO electroreduction on Re-Cu-I (a) and Re-Cu-Cl (d) with CO flow rate of 6 mL/min at potential ranging from -0.26 V to -0.66 V vs. RHE. FE of C₂ products from CO electroreduction on Re-Cu-I (b) and Re-Cu-Cl (e) with CO flow rate of 6 mL/min, 4 mL/min, 2 mL/min at potential ranging from -0.26 V to -0.66 V vs. RHE. (c) Partial current density of C₂ products from CO electroreduction on Re-Cu-I (c) and Re-Cu-Cl (f) with CO flow rate of 6 mL/min, 4 mL/min, 2 mL/min at potential ranging from -0.26 V to -0.66 V vs. RHE.

As the contrast samples, the Re-Cu-Br and Re-Cu-Cl show similar performance for electrochemical CO₂ reduction but display poorer selectivity toward C₂ species compared with Re-Cu-I at the same applied potentials (Fig. 3b, Fig. S18 and Fig. S19). At the selected potential of -0.99V, the FE of C₂ products for Re-Cu-Br and Re-Cu-Cl is 41.3% and 40.2 %, respectively, with the corresponding PCE of 26% and 25%, which is both lower than that of Re-Cu-I (Fig. 3d, Fig. S20 and Fig. S21). As for the EP-Cu, C₁ species (CO and HCOOH) is preferentially produced (Fig. 3d, Fig. S22 and Fig. S23). All the above results highlight that the surface reconstruction by electrochemical oxidation-reduction cycling in the presence of halide anions significantly promote C₂ product formation and the Re-Cu-I exhibits best performance.

Except for the activity and selectivity, the stability is another key parameter to evaluate the catalyst performance. Therefore, the extending electrolysis of Re-Cu-I is performed at -0.99V vs. RHE (Fig. 3e). During continuously electrolyzing for 48 hours, the overall current density gradually decreases from 22.3 mA/cm² to 19.7 mA/cm² but the FE of C₂H₄ is kept above 50% in the whole period. To distinguish whether there is any structural change of the electrode surface, the catalysts after the reaction are characterized by GIXRD, Cu L-edge XAS and SEM equipped with EDS. The in-plane XRD pattern only exhibits the Cu (200) and Cu (220) peaks, suggesting that the oxidized Cu⁺ is reduced during electrocatalytic CO₂ reduction (Fig. S24). Fitting of Cu L-edge XAS spectrum discloses that the electrode after the reaction contains 96% Cu⁰ and 4% Cu⁺ (Fig. S25 and Table S2). The residual Cu⁺ is likely attributed to rapid re-oxidation after removal of reduction potential³⁵. Notably, negligible

morphology change is discerned for the Re-Cu-I after the reaction, as evidenced by the SEM imaging (Fig. S26). The trace amount of O detected by the EDS is consistent with the XAS result.

The electrochemically active surface area (ECSA) of Re-Cu-I, Re-Cu-Br and Re-Cu-Cl is also determined by the double-layer capacitance method to exclude the roughness factor (RF) and facilitate direct comparison of their activity (Fig. S27). The RF of Re-Cu-I, Re-Cu-Br and Re-Cu-Cl is calculated to be 262, 154 and 186, respectively (Fig. S28). After being normalized by the ECSA, the total C₂ partial current density (*j*_{C₂}) of Re-Cu-I is 79 μA/cm² at -1.09 V vs. RHE, which is still 1.3-fold or 1.5-fold of that of Re-Cu-Br and Re-Cu-Cl (Fig. S29).

Why does the Re-Cu-I possess the best electrocatalytic performance towards C₂ products by CO₂ reduction? The electrochemical CO₂ reduction mechanism of all the reconstructed electrodes and EP-Cu is investigated by Tafel analysis. The Tafel plots are drawn by the overpotential (*η*) versus the logarithm of steady-state C₂H₄ partial current density [*log*(*j*_{C₂H₄})] (Fig. 3f). Tafel slope of Re-Cu-Br, Re-Cu-Cl and EP-Cu is determined to be 98 mV/dec, 95 mV/dec and 114 mV/dec by linear fitting of the current density at low potential from -0.79 V to -0.89 V vs. RHE. These values are close to the 119 mV/dec, implying the electron transfer to *CO to form the *OCCO is the rate-determine step (RDS). In sharp contrast, the Tafel slope of Re-Cu-I is calculated to be 76 mV/dec by the same method, demonstrating an improved 2*CO dimerization kinetic³⁶.

It has been reported that Cu (100) facet favors C₂ species production through promoting C-C coupling reaction whereas both Cu(110) facet and corresponding step preferentially



generates CH_4 .³⁷⁻³⁹ In this respect, Re-Cu-Cl and Re-Cu-Br of Cu nanocube structure contain higher percentage of Cu (100) facets compared with Re-Cu-I. However, either the Faradaic selectivity or the Tafel analysis reveals that the Re-Cu-I is more preferable for generating C_2 products. Moreover, considering that all the three electrodes show similar constituents (Cu^0 and Cu^+ , Table S3), the Cu oxidation state is excluded to be the determining factor of different electrocatalytic performance. The grain boundaries or some defect sites can also promote C-C coupling reaction⁴⁰. But the active sites supported by grain boundaries has been reported to prefer to produce CH_3COOH and $\text{CH}_3\text{CH}_2\text{OH}$. The product distribution is quite different from that in Re-Cu-I implying the grain boundaries contribute little to the excellent C_2 selectivity in Re-Cu-I^{8,16,41,42}. The ECSA normalized total C_2 partial current density (j_{C_2}) also demonstrates that the Re-Cu-I exhibits better intrinsic activity toward electrocatalytic CO_2 reduction. As a result, it is reasonable to correlate the electrochemical performances to the porous structure itself rather than surface feature of Cu electrodes. Evidently, the entangled cobweb-like surface structure is achieved for Re-Cu-I after redox reconstruction due to the unique chemical property of I. Thus, we attribute the boosting selectivity toward C_2 products of Re-Cu-I to its hierarchical porous structure, which entrap the key intermediates CO in the interior of the pores and consequently enhance the surface coverage of adsorbed $^*\text{CO}$ for $^*\text{CO}$ - $^*\text{CO}$ dimerization reaction.

To verify the enrichment effect of catalysts, the electrochemical CO reduction reactions with various flow rates are carried out in CO saturated 1M KOH. At the CO flow rate of 6 mL/min, C_2 products of total FE of 19.5% including C_2H_4 , $\text{CH}_3\text{CH}_2\text{OH}$ and CH_3COOH are detected at low onset potential of -0.26 V vs. RHE (Fig. 4a). The FE of C_2H_4 ($\text{FE}_{\text{C}_2\text{H}_4}$) grows rapidly after more negative potential is applied. The optimal value of $\text{FE}_{\text{C}_2\text{H}_4}$ reaches 67.5 % at the potential of -0.56 V vs. RHE. And at this potential, the entire C_2 selectivity (FE_{C_2}) of 85.1% is obtained with a partial current density (j_{C_2}) of 6.7 mA/cm^2 (Fig. 4b and 4c). At more negative potentials, the surface CO coverage depletion induced by the CO transportation limitation causes a decrease of FE_{C_2} . It is clear that the Re-Cu-I is also an excellent catalyst for C_2 species generation in CO reduction.

When the CO flow rate is reduced, the CO reduction activity should be affected due to limited CO supply and the poor CO solubility in aqueous solution. Nevertheless, both of the FE_{C_2} and j_{C_2} only show a slight decrease when the CO flow rate is decreased to 4 mL/min (Fig. 4b, Fig. 4c and Fig. S30a). At the CO flow rate of 2 mL/min, the FE_{C_2} reduces by 22% and j_{C_2} decreases by 20% at -0.56 V (Fig. 4c and Fig. S30b). It demonstrates the CO reduction performance of the Re-Cu-I is independent of CO flow rate to some extent. Under the sufficient CO supply, the Re-Cu-Cl as a typical contrast sample shows FE_{C_2} of 73.4% with j_{C_2} of 4.9 mA/cm^2 (Fig. 4e-4f) at the potential of -0.56 V, and both are lower than that of Re-Cu-I. Furthermore, the FE_{C_2} diminishes by 26% and 56% respectively at CO flow rate of 4 mL/min and 2 mL/min and the j_{C_2} decreases by 31% and 68% (Fig. 4e and Fig. S31). Therefore, it is concluded that the electrocatalytic performance of Re-Cu-Cl is highly dependent on the CO supply.

It has been reported that the enhanced surface coverage of $^*\text{CO}$ will promote the C-C coupling reaction accompanied by suppression of H_2 generation^{43, 44}. In the electrocatalytic CO_2 reduction, the activity and selectivity are highly dependent on the local CO concentration at the electrode surface⁴². Under the CO -rich alkaline condition, the electrocatalytic performance reflects the intrinsic nature of catalyst for C_2 species production other than the effect of pH. The Re-Cu-I displays higher C_2 selectivity and partial current density, highlighting the entangled cobweb-like surface structure is critical for CO dimerization reactions. It is believed that the hierarchical porous structure contributes to enriching CO to maintain the local CO concentration at the electrode surface. As a result, it is reasonable that C_2 evolution activity is much less affected by the CO supply in Re-Cu-I (Fig. 4b and Fig. 4c). Analogously, during the electrochemical CO_2 reduction, the CO is always at a deficient state since the concentration of as-formed $^*\text{CO}$ is low on the surface. However, in the porous structure, the local generated key intermediate CO owns a long and complicated pathway to diffuse out as the final product electrocatalytic CO_2 reduction. Hence, the retention time of CO at the active surface is prolonged and the CO local concentration is enriched in the interior of the pores, which rationally enhance the surface coverage of $^*\text{CO}$ species. Since that the C_2 generation rate has a second-order dependence on the surface coverage of $^*\text{CO}$ ³⁶, the reaction rate for RDS (2^*CO dimerization reaction) would be significantly improved because of the enhanced surface coverage of $^*\text{CO}$ species. In short, the raised surface coverage of $^*\text{CO}$ resulting from CO enrichment inside the hierarchical pores of Re-Cu-I boosts the dominated C_2 production in electrocatalytic CO_2 reduction.

Conclusions

In conclusion, we develop a halide anion assisted electrochemical method to reconstruct the Cu electrode surface for promoting electrocatalytic CO_2 reduction. The highly insoluble nature of CuI facilitates the formation of the entangled Cu nanowires structure on the Cu electrode surface via oxidation-reduction cycling. The resultant hierarchical pores in Re-Cu-I effectively enrich the key $^*\text{CO}$ intermediates for C_2 products evolution. The comprehensive comparison of CO_2 electroreduction performance among Re-Cu-I, Re-Cu-Br and Re-Cu-Cl demonstrates that the surface structure rather than the lattice facet is the determining factor for boosting C_2 products formation. These results distinctly manifest that the interconnected porous structure on the electrode surface is crucial to improve C_{2+} generation by increasing the local CO availability. It is also prospective to achieve the higher C_{2+} selectivity via smartly tuning the pore size.

Conflicts of interest

The authors declare no competing financial interests.



Acknowledgements

The authors acknowledge financial support from National Key Basic Research Program of China (2016YFA0200700, Z.Y.T.), National Natural Science Foundation of China (21890381 and 21721002, Z.Y.T.), Frontier Science Key Project of Chinese Academy of Sciences (QYZDJ-SSW-SLH038, Z.Y.T.), and K.C.Wong Education Foundation (Z.Y.T.).

Author contribution

J.H. and Z.T. conceived and designed this project. J.H. prepared the samples, participated in characterization, and conducted the electrochemical experiments. J.Z., K.H., D.W., Z.Y. and S.Y. joined the discussion of the data and gave useful suggestions. J.H., Y.Y., and Y.Z. participated in the characterization and helped to draft the manuscript. Z.T. supervised and guided the project. All authors commented on the data and the manuscript.

Notes and references

- M. G. Kibria, J. P. Edwards, C. M. Gabardo, C. T. Dinh, A. Seifitokaldani, D. Sinton and E. H. Sargent, *Adv. Mater.*, 2019, **31**, 1807166.
- J. Qiao, Y. Liu, F. Hong and J. Zhang, *Chem. Soc. Rev.*, 2014, **43**, 631-675.
- T.-T. Zhuang, Z.-Q. Liang, A. Seifitokaldani, Y. Li, P. De Luna, T. Burdyny, F. Che, F. Meng, Y. Min, R. Quintero-Bermudez, C. T. Dinh, Y. Pang, M. Zhong, B. Zhang, J. Li, P.-N. Chen, X.-L. Zheng, H. Liang, W.-N. Ge, B.-J. Ye, D. Sinton, S.-H. Yu and E. H. Sargent, *Nat. Catal.*, 2018, **1**, 421-428.
- D. Kim, C. S. Kley, Y. Li and P. Yang, *PNAS*, 2017, **114**, 10560-10565.
- Y. Wang, Z. Wang, C.-T. Dinh, J. Li, A. Ozden, M. Golam Kibria, A. Seifitokaldani, C.-S. Tan, C. M. Gabardo, M. Luo, H. Zhou, F. Li, Y. Lum, C. McCallum, Y. Xu, M. Liu, A. Proppe, A. Johnston, P. Todorovic, T.-T. Zhuang, D. Sinton, S. O. Kelley and E. H. Sargent, *Nat. Catal.*, 2020, **3**, 98-106.
- S. Nitopi, E. Bertheussen, S. B. Scott, X. Liu, A. K. Engstfeld, S. Horch, B. Seger, I. E. L. Stephens, K. Chan, C. Hahn, J. K. Nørskov, T. F. Jaramillo and I. Chorkendorff, *Chem. Rev.*, 2019, **119**, 7610-7672.
- D. Gao, R. M. Arán-Ais, H. S. Jeon and B. Roldan Cuenya, *Nat. Catal.*, 2019, **2**, 198-210.
- C. W. Li and M. W. Kanan, *J. Am. Chem. Soc.*, 2012, **134**, 7231-7234.
- H. Mistry, A. S. Varela, C. S. Bonifacio, I. Zegkinoglou, I. Sinev, Y. W. Choi, K. Kisslinger, E. A. Stach, J. C. Yang, P. Strasser and B. R. Cuenya, *Nat. Commun.*, 2016, **7**, 12123.
- W. Tang, A. A. Peterson, A. S. Varela, Z. P. Jovanov, L. Bech, W. J. Durand, S. Dahl, J. K. Nørskov and I. Chorkendorff, *Phys. Chem. Chem. Phys.*, 2012, **14**, 76-81.
- F. S. Roberts, K. P. Kuhl and A. Nilsson, *Angew. Chem. Int. Ed.*, 2015, **54**, 5179-5182.
- D. Ren, Y. Deng, A. D. Handoko, C. S. Chen, S. Malkhandi and B. S. Yeo, *ACS Catal.*, 2015, **5**, 2814-2821.
- K. Jiang, R. B. Sandberg, A. J. Akey, X. Liu, D. C. Bell, J. K. Nørskov, K. Chan and H. Wang, *Nat. Catal.*, 2018, **1**, 111-119.
- A. D. Handoko, C. W. Ong, Y. Huang, Z. G. Lee, C. Lin, G. B. Panetti and B. S. Yeo, *J. Phys. Chem. C*, 2016, **120**, 20058-20067.
- A. Eilert, F. Cavalca, F. S. Roberts, J. Osterwalder, C. Liu, M. Favaro, E. J. Crumlin, H. Ogasawara, D. Friebe, L. G. Pettersson and A. Nilsson, *J. Phys. Chem. Lett.*, 2017, **8**, 285-290.
- C. W. Li, J. Ciston and M. W. Kanan, *Nature*, 2014, **508**, 504-507.
- K. J. Schouten, Z. Qin, E. Perez Gallent and M. T. Koper, *J. Am. Chem. Soc.*, 2012, **134**, 9864-9867.
- P. De Luna, R. Quintero-Bermudez, C.-T. Dinh, M. B. Ross, O. S. Bushuyev, P. Todorovic, T. Regier, S. O. Kelley, P. Yang and E. H. Sargent, *Nat. Catal.*, 2018, **1**, 103-110.
- Y. Lum and J. W. Ager, *Nat. Catal.*, 2018, **2**, 86-93.
- T.-T. Zhuang, Y. Pang, Z.-Q. Liang, Z. Wang, Y. Li, C.-S. Tan, J. Li, C. T. Dinh, P. De Luna, P.-L. Hsieh, T. Burdyny, H.-H. Li, M. Liu, Y. Wang, F. Li, A. Proppe, A. Johnston, D.-H. Nam, Z.-Y. Wu, Y.-R. Zheng, A. H. Ip, H. Tan, L.-J. Chen, S.-H. Yu, S. O. Kelley, D. Sinton and E. H. Sargent, *Nat. Catal.*, 2018, **1**, 946-951.
- K. D. Yang, W. R. Ko, J. H. Lee, S. J. Kim, H. Lee, M. H. Lee and K. T. Nam, *Angew. Chem. Int. Ed.*, 2017, **56**, 796-800.
- T. T. H. Hoang, S. Verma, S. Ma, T. T. Fister, J. Timoshenko, A. I. Frenkel, P. J. A. Kenis and A. A. Gewirth, *J. Am. Chem. Soc.*, 2018, **140**, 5791-5797.
- C. S. Chen, A. D. Handoko, J. H. Wan, L. Ma, D. Ren and B. S. Yeo, *Catal. Sci. Technol.*, 2015, **5**, 161-168.
- Y. Kwon, Y. Lum, E. L. Clark, J. W. Ager and A. T. Bell, *ChemElectroChem*, 2016, **3**, 1012-1019.
- H. Yano, T. Tanaka, M. Nakayama and K. Ogura, *J. Electroanal. Chem.*, 2004, **565**, 287-293.
- S. Huemann, N. T. Minh Hai, P. Broekmann, K. Wandelt, H. Zojonz, H. Dosch and F. Renner, *J. Phys. Chem. B*, 2006, **110**, 24955-24963.
- F. A. Akgul, G. Akgul, N. Yildirim, H. E. Unalan and R. Turan, *Mater. Chem. Phys.*, 2014, **147**, 987-995.
- L. Martin, H. Martinez, D. Poinot, B. Pecquenard and F. Le Cras, *J. Phys. Chem. C*, 2013, **117**, 4421-4430.
- M. G. Kibria, C. T. Dinh, A. Seifitokaldani, P. De Luna, T. Burdyny, R. Quintero-Bermudez, M. B. Ross, O. S. Bushuyev, F. P. Garcia de Arquer, P. Yang, D. Sinton and E. H. Sargent, *Adv. Mater.*, 2018, **30**, 1804867.
- D. Gao, I. Zegkinoglou, N. J. Divins, F. Scholten, I. Sinev, P. Grosse and B. Roldan Cuenya, *ACS Nano*, 2017, **11**, 4825-4831.
- T. T. H. Hoang, S. Ma, J. I. Gold, P. J. A. Kenis and A. A. Gewirth, *ACS Catal.*, 2017, **7**, 3313-3321.
- Y. Zhou, F. Che, M. Liu, C. Zou, Z. Liang, P. De Luna, H. Yuan, J. Li, Z. Wang, H. Xie, H. Li, P. Chen, E. Bladt, R. Quintero-Bermudez, T. K. Sham, S. Bals, J. Hofkens, D. Sinton, G. Chen and E. H. Sargent, *Nat. Chem.*, 2018, **10**, 974-980.
- J. Kim, W. Choi, J. W. Park, C. Kim, M. Kim and H. Song, *J. Am. Chem. Soc.*, 2019, **141**, 6986-6994.
- F. Li, A. Thevenon, A. Rosas-Hernandez, Z. Wang, Y. Li, C. M. Gabardo, A. Ozden, C. T. Dinh, J. Li, Y. Wang, J. P. Edwards, Y. Xu, C. McCallum, L. Tao, Z. Q. Liang, M. Luo, X. Wang, H. Li, C. P. O'Brien, C. S. Tan, D. H. Nam, R. Quintero-Bermudez, T. T. Zhuang, Y. C. Li, Z. Han, R. D. Britt, D. Sinton, T. Agapie, J. C. Peters and E. H. Sargent, *Nature*, 2020, **577**, 509-513.
- Y. Lum and J. W. Ager, *Angew. Chem. Int. Ed.*, 2018, **57**, 551-554.
- X. Liu, P. Schlexer, J. Xiao, Y. Ji, L. Wang, R. B. Sandberg, M. Tang, K. S. Brown, H. Peng, S. Ringe, C. Hahn, T. F. Jaramillo, J. K. Nørskov and K. Chan, *Nat. Commun.*, 2019, **10**, 1-10.



- 2019, **10**, 32.
37. Y. Huang, A. D. Handoko, P. Hirunsit and B. S. Yeo, *ACS Catal.*, 2017, **7**, 1749-1756.
38. K. J. P. Schouten, E. Pérez Gallent and M. T. M. Koper, *ACS Catal.*, 2013, **3**, 1292-1295.
39. I. Takahashi, O. Koga, N. Hoshi and Y. Hori, *J. Electroanal. Chem.*, 2002, **533**, 135-143.
40. Y. Huang, Y. Chen, T. Cheng, L.-W. Wang and W. A. Goddard, *Acs Energy Lett.*, 2018, **3**, 2983-2988.
41. A. Verdaguier-Casadevall, C. W. Li, T. P. Johansson, S. B. Scott, J. T. McKeown, M. Kumar, I. E. Stephens, M. W. Kanan and I. Chorkendorff, *J. Am. Chem. Soc.*, 2015, **137**, 9808-9811.
42. X. Feng, K. Jiang, S. Fan and M. W. Kanan, *ACS Cent. Sci.*, 2016, **2**, 169-174.
43. J. Li, Z. Wang, C. McCallum, Y. Xu, F. Li, Y. Wang, C. M. Gabardo, C.-T. Dinh, T.-T. Zhuang, L. Wang, J. Y. Howe, Y. Ren, E. H. Sargent and D. Sinton, *Nat. Catal.*, 2019, **2**, 1124-1131.
44. Y. Huang, A. D. Handoko, P. Hirunsit and B. S. Yeo, *ACS Catal.*, 2017, **7**, 1749-1756.

View Article Online
DOI: 10.1039/D0SC01202E

